Local Demagnetization Fault Recognition of Permanent Magnet Synchronous Linear Motor Based on S-Transform and PSO–LSSVM

Xuewei Song, Jiwen Zhao, Juncai Song, Fei Dong, Liang Xu, and Jing Zhao

***Abstract*—This article focuses on the local demagnetization fault recognition research of permanent magnet synchronous linear motor (PMSLM) and realizes the accurate identification of the position and degree of demagnetized permanent magnets. A fault recognition system based on S-transform (ST) and particle swarm optimization–least squares support vector machine (PSO–LSSVM) is proposed. The ST makes the induced electromotive force (EMF) signal with stronger signal characteristic expression ability, and the PSO–LSSVM model achieves better generalization ability and higher accuracy in the small sample state of PMSLM faults. In the process of fault identification: 1) the induced EMF analytical model for PMSLM under local demagnetization fault is presented; 2) the induced EMF signal is analyzed by ST, and the characteristic parameters are extracted from time–frequency curves. Then a characteristic vector is established by comparing the standard deviation values and similarities of different parameters; 3) a PSO–LSSVM classification model is established to realize the recognition of PMSLM faults. Prototype and finite element simulation experimental results confirm that the method can recognize the PMSLM faults accurately with a recognition rate of 100%.**

***Index Terms*—Induced electromotive force (EMF), particle swarm optimization–least squares support vector machine (PSO–LSSVM), permanent magnet synchronous linear motor (PMSLM), S-transform (ST).**

I. Introduction

PERMANENT magnet synchronous linear motor (PMSLM) has the characteristic such as direct driving, high positioning precision, and low noise [1], [2]. Therefore, it is widely used in laser cutting machines, glass substrate testing equipment, and other high-grade computer numerical control machines [3]–[5].

However, the industrial environment leads to irreversible demagnetization of some permanent magnets (PMs) under the influence of the external magnetic field, high temperature, chemical corrosion, and natural aging [6]–[8]. When the PMSLM is locally demagnetized, the thrust fluctuation is increased and the operation reliability is decreased [9]. Ultimately, the output performance of high-precision machines is reduced, which affects the processing accuracy of products. Therefore, in industrial applications, an effective fault diagnosis method is needed to accurately identify the position and degree of demagnetized permanent magnets.

In permanent magnet synchronous motor demagnetization fault diagnosis methods, the fault characteristic parameters are mainly extracted from voltage [10]–[12], current [13]–[15], and magnetic signals [16]–[18]. The signal analysis methods are generally divided into three categories.

1) Use Wavelet transforms (WTs), Hilbert-Huang (HHT), and other methods to analyze current and voltage signals.
2) Obtain the PMs flux global information quantitatively by model analysis.
3) Construct the PMs flux online observer to diagnose motor demagnetization faults.

In the existing literature, WT [19] has variable time–frequency resolution, but it is susceptible to noise; HHT [20] has mode aliasing and fails to describe the time–frequency characteristics accurately. The finite element model [17] is effective for achieving qualitative and quantitative information, but it is a physical model with a large amount of calculation; PMs flux linkage online observer [18] can provide accurate quantitative parameters, but the result is greatly affected by the measurement noise, thereby causing misdiagnosis of motor faults.

Therefore, a method with a small calculation amount, strong anti-noise capability, and accurate fault characteristic parameters extraction is needed for PMSLM local demagnetization fault diagnosis. The S-transform (ST) is originated from the short-time Fourier transform or the WT, which has strong applicability with good signal characteristics performance. In the literature [21], ST is used to realize fault diagnosis for power quality, it can effectively extract the time–frequency characteristic parameters from current with small calculation amount. The research work shows that ST has the advantages of variable time–frequency resolution, fine decomposition of frequency domain, and good noise immunity [22]–[24].

The models used for fault classification mainly include neural networks [25], support vector machine (SVM) [26], and decision trees [27]. The least square support vector machine (LSSVM)

Manuscript received June 27, 2019; revised September 9, 2019 and December 5, 2019; accepted January 12, 2020. Date of publication January 15, 2020; date of current version April 22, 2020. This work was supported by the National Natural Science Foundation of China under Grant 51837001, Grant 51637001, Grant 51707002, and Grant 51577001. Recommended for publication by Associate Editor S. K. Mazumder. *(Corresponding author: Jiwen Zhao.)*

X. Song is with the Environment Oriented Information and System Engineering, the Graduate School, Mie University, Mie 514-8507, Japan (e-mail: tianya0218s@126.com).

J. Zhao and J. Song are with the School of Electrical and Automation Engineering, Hefei University of Technology, Hefei 230009, China (e-mail: ustczjw@ahu.edu.cn; songjuncai528@gmail.com).

F. Dong, L. Xu, and J. Zhao are with the School of Electrical Engineering and Automation, Anhui University, Hefei 230601, China (e-mail: 496395060@qq.com; 2390290032@qq.com; 247532029@qq.com).

Color versions of one or more of the figures in this article are available online at https://ieeexplore.ieee.org.

Digital Object Identifier 10.1109/TPEL.2020.2967053

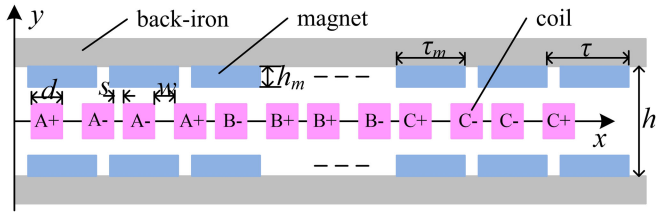

Fig. 1. Layer analysis model of PMSLM.

TABLE I
MAIN STRUCTURE PARAMETERS OF PMSLM DESIGN

Parameters	Description
τ	pole pitch
τ_m	magnet width
h_m	magnet thickness
h	distance between two back irons
d	single wires width
w	distance between two wires
s	distance between two coils

[28] is the extension of SVM, it has the advantages of strong generalization and small sample problem processing abilities and can solve problems of a small sample and nonlinear and local minima. The particle swarm optimization (PSO) [29] algorithm has a strong global search ability and can be used to solve the global optimization problem of LSSVM parameters.

In this study, the induced EMF is taken as the fault signal, the ST is used to extract the time–frequency parameters for constructing the characteristic vector, and PSO–LSSVM algorithm is used to establish the classification recognition model. The advantages and novelties of the proposed PMSLM local demagnetization faults recognition system are summarized as follows:

1) ST has good time–frequency resolution, which makes the performance of fault characteristics more obvious.
2) Based on standard deviation (STD) values and similarity calculation, the dimension of the characteristic vector is reduced.
3) The method of identifying faults hierarchically improves the recognition accuracy of the PSO–LSSVM model.
4) The experiment verifies that the method has strong anti-noise ability, small calculation amount, and high detection precision.

The rest of the article is organized as follows. Section II introduces the PMSLM local demagnetization fault model; Section III describes the characteristic vector extraction process based on ST in detail; Section IV contains the PSO–LSSVM recognition model; Section V contains the experimental results; and Section VI summarizes the conclusion.

II. LOCAL DEMAGNETIZATION FAULT MODEL OF PMSLM

A. Analytical Model

Fig. 1 shows the layer analysis model of a bilateral PMSLM, and Table I shows the meaning of each parameter.

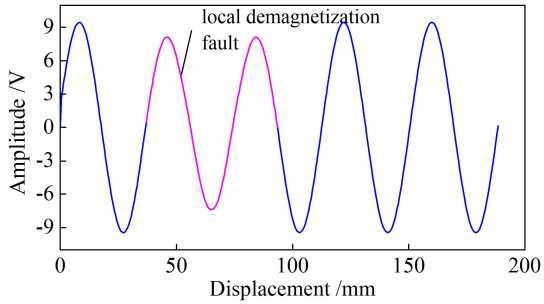

Fig. 2. Induced EMF analytic waveform.

In accordance with equivalent magnetization method, the flux density of air gap [4] is given by

$$B_y(x) = \sum_{n=1}^{\infty} \frac{4B_r(x)}{(2n-1)\pi} \frac{\sin h\left((2n-1)\pi \frac{h_m}{\tau}\right)}{\sin h\left(\frac{(2n-1)\pi}{2}\frac{h}{\tau}\right)} \times \sin\frac{(2n-1)\pi}{2} \sin\left(\frac{(2n-1)\pi}{2}\frac{\tau_m}{\tau}\right) \times \cosh\left(\frac{(2n-1)\pi}{\tau}y\right) \sin\left(\frac{(2n-1)\pi}{\tau}x\right) \quad (1)$$

where $B_r(x)$ is a piecewise function that represents the residual magnetization at x coordinates.

The a-phase induced electromotive force (EMF) is given by

$$E_a = 2\left(E_{A+} - E_{A-}\right) = \mathrm{NLV}\left[\left(\frac{\int_x^{x+d} B_y dx}{d} - \frac{\int_{x+d+w}^{x+2d+w} B_y dx}{d}\right) - \left(\frac{\int_{x+3d+2w+s}^{x+4d+2w+s} B_y dx}{d} - \frac{\int_{x+2d+w+s}^{x+3d+w+s} B_y dx}{d}\right)\right] \quad (2)$$

where N, L, and V are the number of wires in each phase, the effective length of coils, and the speed of PMSLM.

Equation (2) shows that the change in the average magnetic density determines the changing trend of the induced EMF. Fig. 2 shows the corresponding analytic waveform of (2) when one pair of PMs demagnetized. It can be found that the induced EMF changes over a plurality of cycles, and the difference in amplitude are large. The period of the induced EMF change is inextricably linked with the demagnetization region of the PMs.

B. Fault Type

The induced EMF has been changing since the winding enters the demagnetization region until it completely passes through it. If the winding enters a demagnetization region when it does not completely pass through the previous, the induced EMF will be continues change. Based on the previous study, the conclusions are summarized as follows:

1) When there are three pairs of normal PMs between one demagnetization region and another, the induced EMF changes intermittently.
2) On the influence of induced EMF, when the upper PM and the lower PM in a pair of poles are demagnetized, respectively, they can be equivalent to the state that a pair

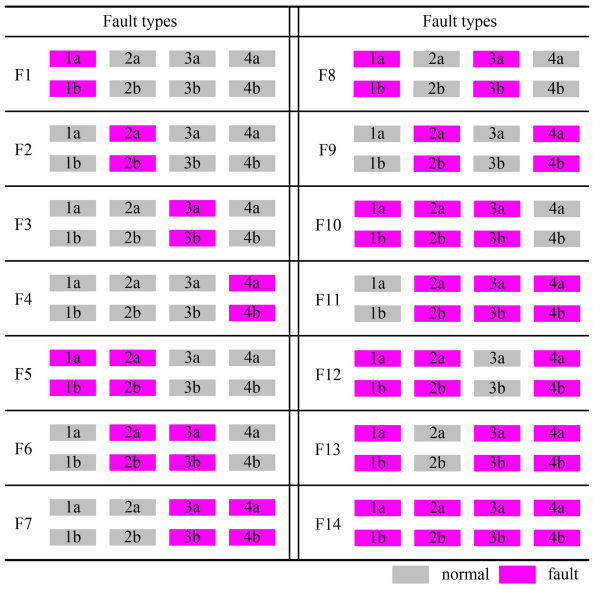

Fig. 3. Demagnetization fault types.

of polar PMs demagnetized, except the demagnetization degree of the PMs are different.

3) Under the same fault type, the demagnetization degree of PMs is different, only the magnitude of induced EMF force is changed.

Therefore, four pairs of PMs in two cycles were selected for PMSLM local demagnetization fault research, which can cover the main fault types. It assumes that the demagnetization degree of the PMs in each fault is the same. Fig. 3 shows the location of demagnetization PMs under 14 fault types.

III. Establishment of Characteristic Factor

A. ST and Application

For the signal processing of the induced EMF, it is required to have good nondestructive, anti-noise, and high resolution. The ST [30] originates from the short-time Fourier transform, and introduces multi-resolution analysis of WT, which has the detailed decomposition and high time–frequency resolution.

The ST of a time signal $x(t)$ can be given as [31]–[33]

$$\begin{cases} S(\tau, f) = \int_{-\infty}^{\infty} x(t) \frac{|f|}{\sqrt{2\pi}} e^{-\frac{(\tau-t)^2 f^2}{2}} e^{-i2\pi f t} dt \\ S(\tau, 0) = \lim\limits_{T\to\infty} \int_{-\frac{T}{2}}^{\frac{T}{2}} x(t) dt. \end{cases} \tag{3}$$

For the sampled induced EMF signal, where N is the total sample points and T is the discrete sampling interval

$$\{x[kT] | k = 0, 1, 2 \ldots N-1\}. \tag{4}$$

The corresponding ST modular matrix (STMM) as

$$S[u, v] = \begin{bmatrix} S_{0,1} & \cdots & S_{0,N-1} \\ \vdots & \ddots & \vdots \\ S_{\frac{N}{2},1} & \cdots & S_{\frac{N}{2},N-1} \end{bmatrix} \tag{5}$$

where $u = jT, v = n/NT$, and $j, n = 0, 1, \ldots, N\text{-}1$.

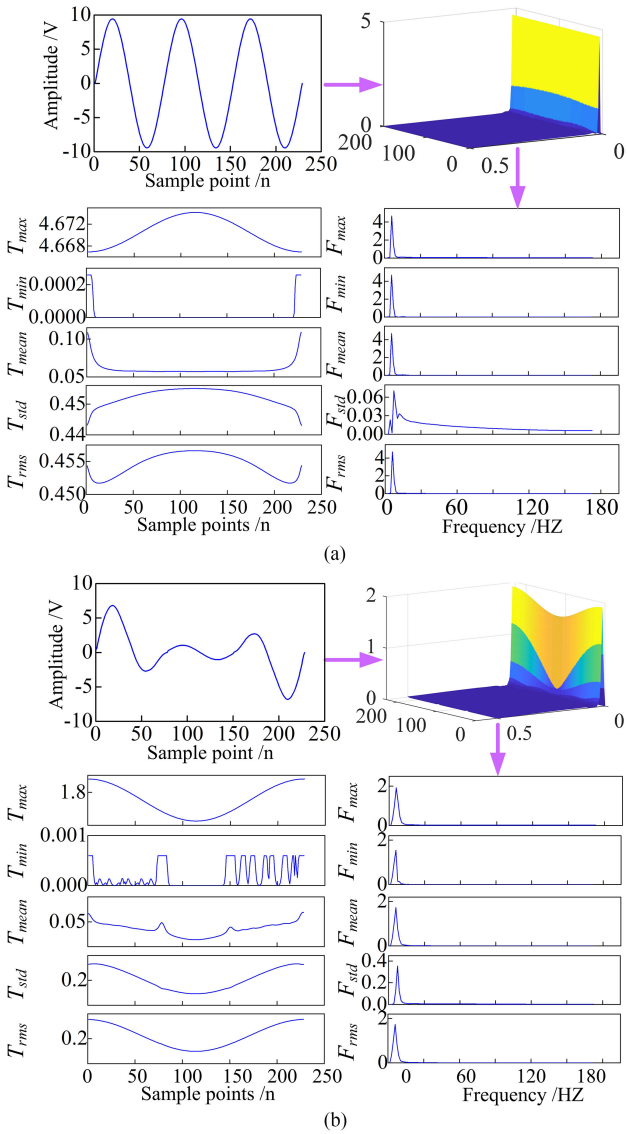

Fig. 4. Induced EMF curves, STMM and time–frequency curves. (a) Normal state. (b) PMSLM local demagnetization fault state.

Extract the maximum value (max), minimum value (min), mean value (mean), std value, root mean square value (rms) of each row and column from the STMM to set up time–frequency curves. $T_{\max}$ curves and $F_{\max}$ curves can be represented by (6) and (7), other curves are similar too

$$T_{\max} = [\max(S[u, 0]), \max(S[u, 1]), \ldots \max(S[u, N])] \tag{6}$$

$$F_{\max} = \left[\max(S[0, v]), \max(S[1, v]), \ldots \max\left(S\left[\frac{N}{2}, v\right]\right)\right]. \tag{7}$$

Fig. 4 shows the STMM and time–frequency curves under normal and fault state, it can be seen that the degree of distortion is inconsistent, and the time–frequency characteristic curves differ significantly.

Therefore, the max, min, mean, std, and rms were extracted from the time–frequency curves to form the characteristic vector. Table II shows the parameters t_1–t_{50}.

TABLE II
ORIGINAL CHARACTERISTIC PARAMETERS

parameter	*max+min*	*max-min*	*mean*	*std*	*rms*
T_{max}	t_1	t_2	t_3	t_4	t_5
T_{min}	t_6	t_7	t_8	t_9	t_{10}
T_{mean}	t_{11}	t_{12}	t_{13}	t_{14}	t_{15}
T_{std}	t_{16}	t_{17}	t_{18}	t_{19}	t_{20}
T_{rms}	t_{21}	t_{22}	t_{23}	t_{24}	t_{25}
F_{max}	t_{26}	t_{27}	t_{28}	t_{29}	t_{30}
F_{min}	t_{31}	t_{32}	t_{33}	t_{34}	t_{35}
F_{mean}	t_{36}	t_{37}	t_{38}	t_{39}	t_{40}
F_{std}	t_{41}	t_{42}	t_{43}	t_{44}	t_{45}
F_{rms}	t_{46}	t_{47}	t_{48}	t_{49}	t_{50}

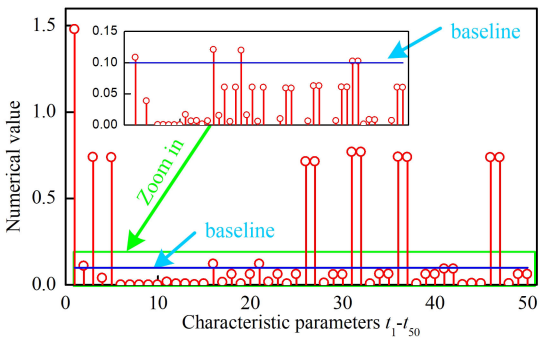

Fig. 5. STD value distribution of characteristic parameters t_1–t_{50}.

B. Screening Characteristic Parameters

1) STD Preliminary Screening: In this article, the PMSLM local demagnetization faults are classified to 14 types

$$F_i \in [F_1, F_2, \ldots F_{14}]. \tag{8}$$

For the characteristic parameters

$$t_j \in [t_1, t_2, \ldots t_{50}]. \tag{9}$$

x_{jF_i} is used to represent the value of the characteristic parameter t_j extracted in the F_i fault state.

Then, the STD of the characteristic parameter t_i can be expressed as follow:

$$\sigma_j = \sqrt{\frac{1}{14}\sum_{i=1}^{14}\left(x_{jF_i} - \bar{x}\right)^2}. \tag{10}$$

Therefore, Fig. 5 shows the distribution of STD values σ_1 to σ_{50} corresponding to 50 characteristic parameters.

The smaller the STD value is, the smaller the difference of the data in the same group will be, and the lower the recognition degree of characteristic parameters will be. Therefore, the characteristic parameters with the STD value less than 0.1 are removed through a preliminary screening. After preliminary screening, a total of 16 characteristic parameters are chosen as follows:

$$\{t_1, t_2, t_3, t_5, t_{16}, t_{21}, t_{26}, t_{27}, t_{31}, t_{32}, t_{36}, t_{37}, t_{41}, t_{42}, t_{46}, t_{47}\}.$$

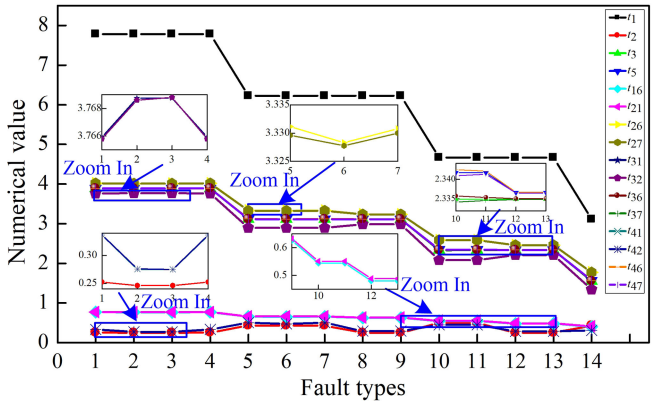

Fig. 6. Characteristic parameters distribution under 14 fault types.

TABLE III
CHARACTERISTIC VECTOR PARAMETERS

Parameter	*Characteristic Parameters*
T_{max}	$10*t_1$, $100*t_2$, $10*t_3$, t_{51},t_{52}
T_{std}	$100*t_{16}$
F_{max}	$10*t_{26}$
F_{min}	$10*t_{31}$
F_{std}	$10*t_{41}$

2) Characteristic Parameters Similarity Screening: The distribution curves of the characteristic parameters under different fault states are analyzed. The values of the corresponding characteristic parameters in the $F1$–$F14$ fault state are sequentially extracted, and the curve t_1 is composed of points

$$\{(F_i, t_1)\,|i = 1, 2, 3 \cdots 14\}. \tag{11}$$

Then draw the other curves in turn, as shown in Fig. 6. It can be seen that the numerical value curves of the 16 characteristic parameters are roughly divided into three regions. A clear distinction is found between the t_1 curve and other curves. Although the numerical value of the t_2 curve is small, it can be clearly distinguished from others. The characteristic parameter curves of t_3, t_5, t_{36}, t_{37}, t_{46}, and t_{47} nearly coincide. The same situation occurs at t_{16} and t_{21}, t_{26} and t_{27}, t_{31} and t_{32}, and t_{41} and t_{42} curves. Therefore, only one characteristic parameter is selected among other similar characteristic parameters to reduce the redundancy of the characteristic vector. Finally, seven characteristic parameters, t_1, t_2, t_3, t_{16}, t_{26}, t_{31}, and t_{41}, are selected to construct the fault characteristic vector.

3) Establishment of Characteristic Vector: Due to the small differences between some fault types, the characteristic parameter values are difficult to distinguish and easily misidentified. Therefore, the max and min value position parameters are extracted from the $T_{\max}$ curve as the characteristic parameters t_{51} and t_{52}. At the same time, the other characteristic parameters are expanded by different multiples. Table III shows the characteristic vector parameters.

Based on the above-mentioned analysis, the characteristic parameters in normal and 14 fault states (the PMs demagnetized

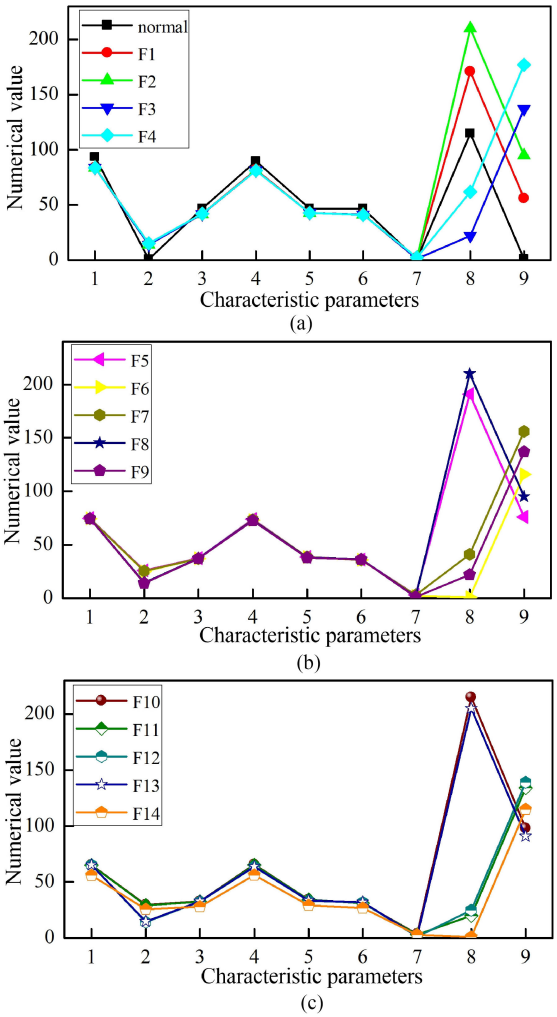

Fig. 7. Characteristic parameter curves under normal and fault states. (a) Normal and fault $F1$–$F4$. (b) Fault $F5$–$F9$. (c) Fault $F10$–$F14$.

degree is 60%) are extracted in turn, as shown in Fig. 7. It can be seen that under the same demagnetization degree, the curve distributions in various fault states are different, which can accurately distinguish the PMSLM local demagnetization fault. In the same picture, when the number of demagnetized PMs is the same, the difference between the characteristic parameters t_1, t_2, t_3, t_{16}, t_{26}, t_{31}, and t_{41} is small, indicating that the similar faults have similarities, but the characteristic parameters t_{51} and t_{52} can be used to distinguish the positions of the demagnetized PMs. Comparing Fig. 7(a)–(c), when the number of demagnetized PMs is different, the difference in characteristic parameters is obvious.

4) Recognition of the Degree of Demagnetization: Aiming at the problem of demagnetization degree in PMSLM local demagnetization fault, the relationship between the characteristic parameters under different demagnetization degrees and complete demagnetization is analyzed. The formula describing the ratio relationship is given as follows:

$$d_j = \frac{t_j}{t_{js}} \tag{12}$$

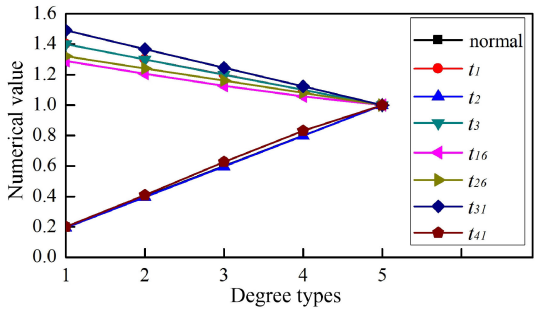

Fig. 8. Ratio results between the characteristic parameters.

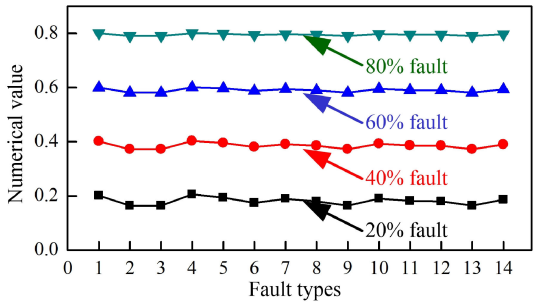

Fig. 9. Identification of demagnetization degree in different fault state.

where t_{js} is the characteristic parameter value when the permanent magnets are completely demagnetized, and t_j is that under various demagnetization degrees.

The specific ratio results of F5 between the characteristic parameters are shown in Fig. 8. It can be seen that the characteristic parameters t_2 and t_{41} can indicate the degree of demagnetization of the PMs, but the characteristic parameter t_2 is more consistent with the true value.

Fig. 9 shows the recognition results of the characteristic parameter t_2 for the degree of demagnetization under different fault states. It can be seen that the characteristic parameter t_2 can accurately identify the demagnetization degree, and the greater the demagnetization degree, the higher the recognition accuracy.

IV. Fault Identification Based on PSO–LSSVM

A. PSO–LSSVM

The PMSLM local demagnetization fault classification model requires good generalization ability, high accuracy, and fast operation speed in a small sample. The PSO algorithm is used to optimize the regularization parameters and kernel function width of LSSVM to improve the accuracy of the classification model.

The formula for learning samples is as follows [28]:

$$T = \{(\boldsymbol{x}_i, y_i) \,|i = 1, 2, 3 \ldots n\}. \tag{13}$$

The regression function of LSSVM is as follows:

$$y = \sum_{i=1}^{n} \alpha_i K(\boldsymbol{x}, \boldsymbol{x}_i) + b \tag{14}$$

where $K(\boldsymbol{x}, \boldsymbol{x}_i) = e^{-\frac{\|\boldsymbol{x}-\boldsymbol{x}_i\|}{2\sigma^2}}$.

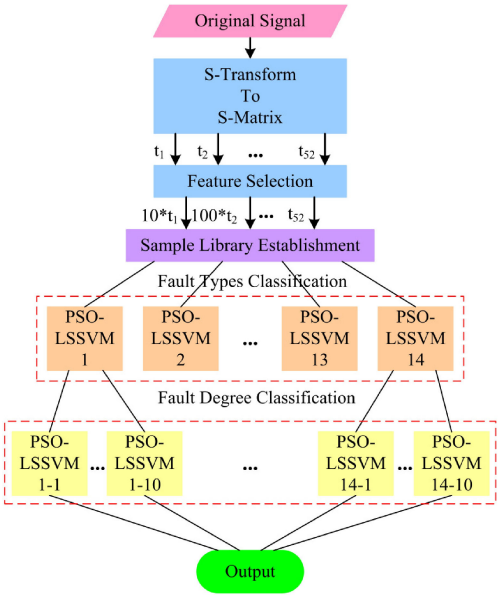

Fig. 10. Fault recognition model based on PSO–LSSVM.

Moreover, σ^2, b, and α_i are the kernel function width, offset, and Lagrange factor, respectively.

The corresponding Lagrange function is as follows:

$$L(\boldsymbol{\omega}, b, \xi, \alpha) = J(\boldsymbol{\omega}, \xi) - \sum_{i=1}^{n} \alpha_i \left(\boldsymbol{\omega}^T \mathrm{g}\boldsymbol{x}_i + b + \xi_i - y_i\right) \tag{15}$$

where ω, ξ_i, and γ are the weight vector, relaxation factor, and regularization parameters, respectively.

The PSO algorithm [29] is as follows:

$$v_{id}^{k+1} = v_{id}^{k} + c_1 r_1^k \left(p_{id}^k - x_{id}^k\right) + c_2 r_2^k \left(p_{gd}^k - x_{gd}^k\right) \tag{16}$$

$$x_{id}^{k+1} = x_{id}^{k} + v_{id}^{k+1}, d = 1, 2, 3 \ldots \tag{17}$$

where i, d, and k are the number of particles, the dimension of the particle, and the number of iterations, respectively; v_{id}^k is the velocity of particle i; x_{id}^k is the position of particle i; p_{id}^k is the optimal position of particle i; p_{gd}^k is the global optimal position of the entire community; c_1 and c_2 are learning factors; r_1 and r_2 are random numbers in the range [0,1].

B. Fault Recognition Model

Fig. 10 shows the fault recognition model based on PSO–LSSVM algorithm designed for the PMSLM local demagnetization fault. First, for the original induced EMF signal, the ST is used to extract the time–frequency characteristic parameters. Second, the characteristic parameters are screened to construct the characteristic vector. Last, the classification model is established on the basis of PSO–LSSVM. The fault types are distinguished first, and then the demagnetization degree is differentiated.

TABLE IV
PMSLM FINITE ELEMENT MODEL PARAMETERS

Parameters		Numerical
PMs	length (mm)	40
	width (mm)	14
	height (mm)	2.5
	magnetization (T)	1.23
coils	number of turns	200
pole pitch (mm)		18
air gap spacing (mm)		1.5
current (A)		2.2*1.414*sin(2*1.414*26.316*time)
running speed (m/s)		1

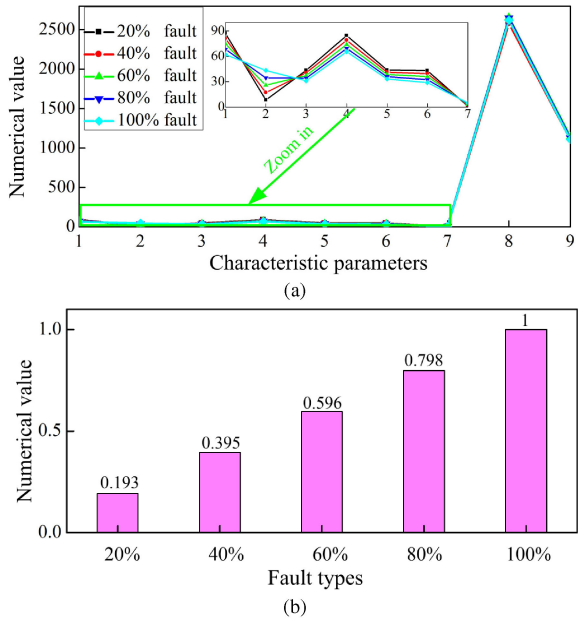

Fig. 11. Test results under different degrees of fault demagnetization. (a) Characteristic parameter curves under different degrees of fault demagnetization. (b) Results of the t_2 characteristic parameter tested.

V. EXPERIMENTAL AND RESULT ANALYSIS

A. Simulation Experiment

The ANSYS Maxwell software is used to establish the PMSLM local demagnetization fault model, the specific parameters are shown in Table IV. In this study, the residual magnetization parameters of the PMs were changed to complete the simulation experiment of the PMs demagnetized degree.

1) Verification of the Degree of Demagnetization PMs: In the F5 fault, five types of demagnetization degrees of PMs are set as 20%, 40%, 60%, 80%, and 100%. The characteristic parameters of each type are extracted and the ratio results are expressed by curves. Fig. 11(a) shows the characteristic parameters curves under different demagnetization degree state, it can be seen that under the same fault, the characteristic parameters curves have a similar pattern. Fig. 11(b) shows the corresponding ratio results of (8), it shows that the characteristic parameter t_2 can accurately indicate the demagnetization degree.

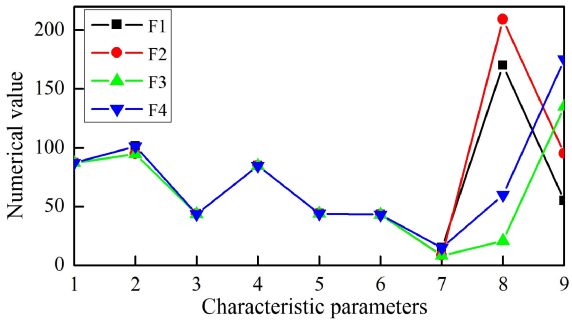

Fig. 12. Characteristic parameter curves of $F1$–$F4$.

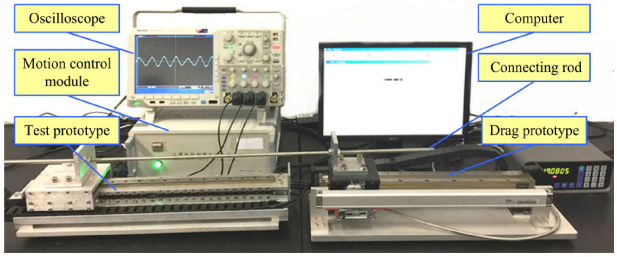

Fig. 13. Induced EMF acquisition experimental platform.

2) Verification of the Position of Demagnetization PMs: In order to verify the method can effectively identify the position of demagnetized PMs, the simulation experiments are carried out on the $F1$–$F4$ fault under the same demagnetization degree. The corresponding characteristic parameters are extracted, as shown in Fig. 12.

Fig. 12 shows that among the 9 characteristic parameters extracted from fault $F1$–$F4$, the corresponding values of characteristic parameters t_1, t_2, t_3, t_{16}, t_{26}, t_{31}, and t_{41} are almost the same, with little difference. Parameters t_{51} and t_{52}, which represent the demagnetization position of PMs, are obviously different. It proved that when the number and form of demagnetizing PMs are the same, the change trend of corresponding induced EMF is the same, and the characteristic parameters t_1, t_2, t_3, t_{16}, t_{26}, t_{31}, and t_{41} obtained after ST are nearly the same. When the demagnetization position of PMs is different, the initial period of induced EMF changes is different, and the position characteristic parameters t_{51} and t_{52} extracted after ST are different. Therefore, this method can accurately identify the position of demagnetization PMs.

B. Prototype Experiment

The experimental platform is set up to verify the effectiveness of the proposed method for PMSLM local demagnetization fault recognition. This platform is shown in Fig. 13, which consists of a test prototype, drag prototype, connecting rod, motion control module, oscilloscope, and computer.

The detail experiment process is as follows: the motion control module of DSP28335 drives the drag prototype moving at a constant speed 1 m/s. In the meanwhile, the test prototype moving synchronously with the drag prototype through the connecting rod, and the induced EMF is generated in the coils.

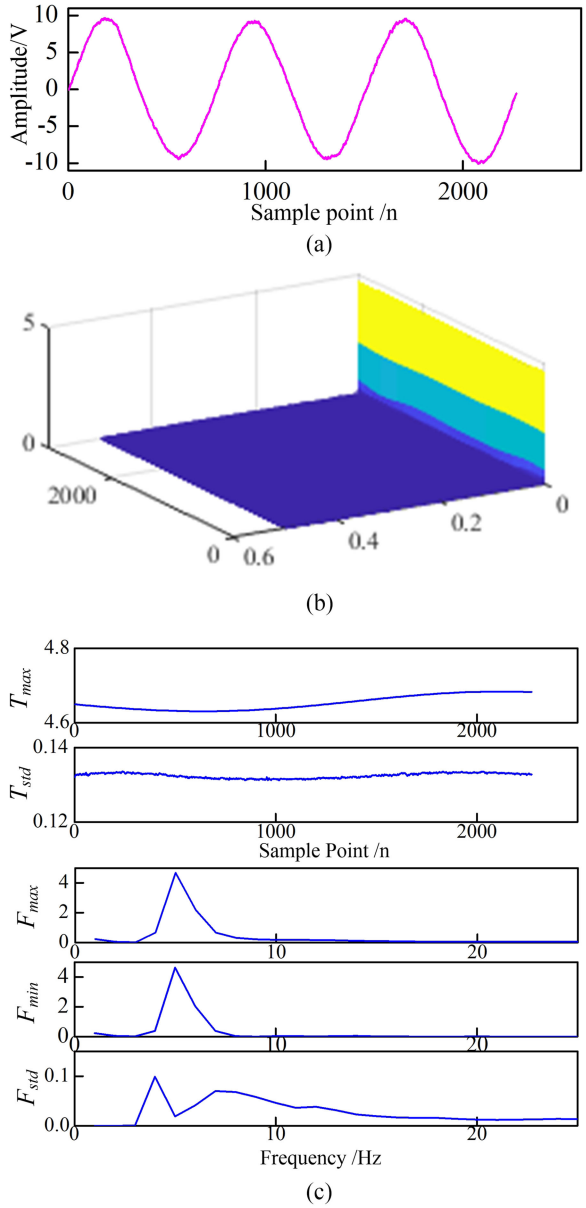

Fig. 14. Induced EMF curves, ST-modular matrix curves, and corresponding time–frequency curves under normal state.

The oscilloscope is used to collect the data of induced EMF, the computer is used to process the data and complete the identification of the PMSLM local demagnetization fault. The induced EMF, ST-modular matrix curves, and corresponding time–frequency curves of the PMSLM under normal state are shown in Fig. 14.

1) Verification of Demagnetization Type: In the prototype verification test, the PMSLM complete demagnetization fault state was expressed by removing the corresponding PMs. Fig. 15 shows the measured induced EMF waveforms and the corresponding ST characteristic parameters curves for the six fault states. After the ST of the original induced EMF signal, the time–frequency characteristics can be clearly presented. The curves under various fault states change considerably, which facilitates the extraction of fault characteristic parameters.

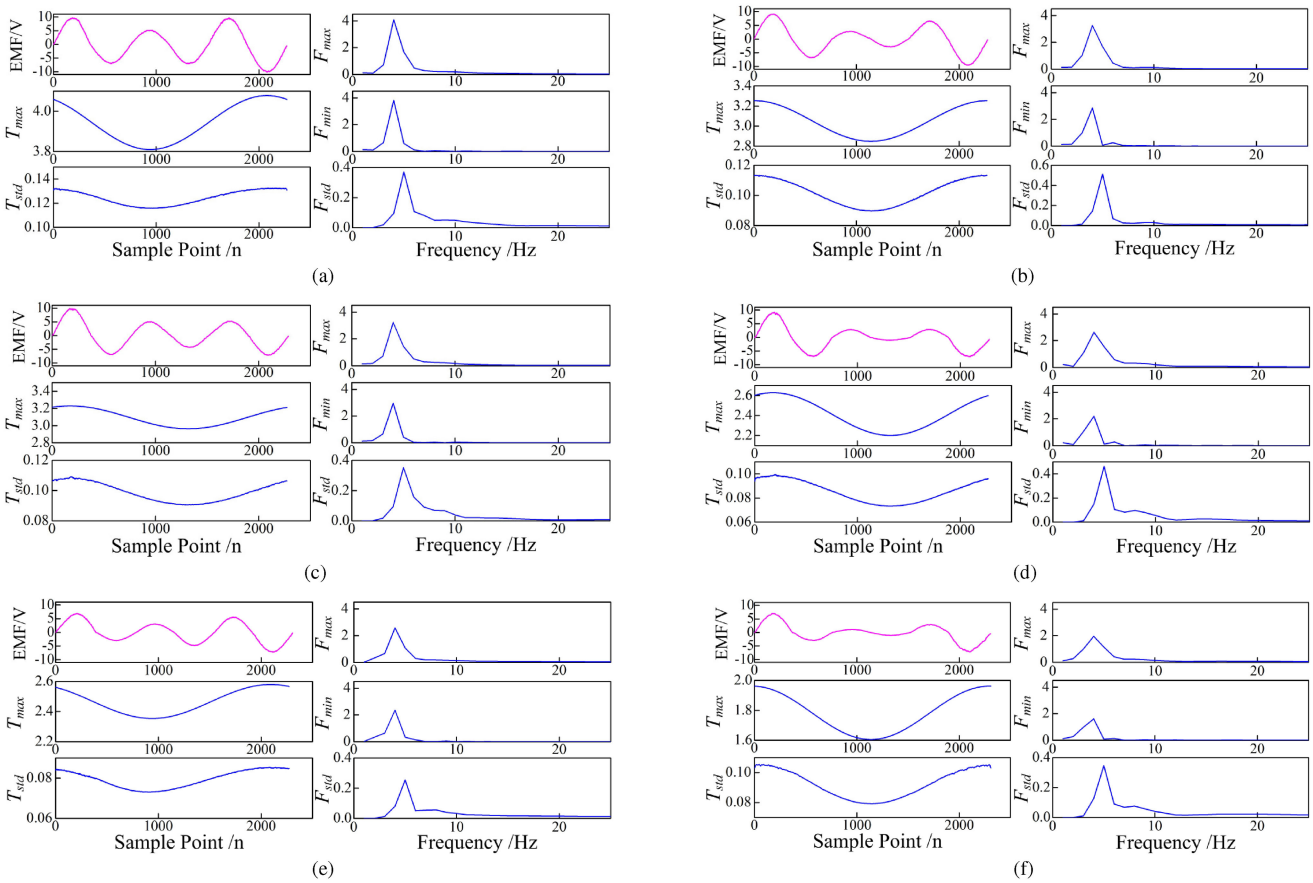

Fig. 15. Corresponding characteristic curves of six fault types. (a) Fault type F2. (b) Fault type F6. (c) Fault type F9. (d) Fault type F11. (e) Fault type F12. (f) Fault type F14.

TABLE V
MEASURED CHARACTERISTIC PARAMETERS OF NORMAL AND SIX FAULT TYPES

parameter	Type						
	normal	F2	F6	F9	F11	F12	F14
$10t_1$	93.1	78.8	61.0	61.9	48.2	49.3	35.6
$100t_2$	5.3	26.8	40.4	26.5	42.6	22.5	35.7
$10t_3$	46.5	39.4	30.5	30.9	24.1	24.6	17.8
$100t_{16}$	26.5	24.8	20.3	19.9	17.2	15.8	18.4
$10t_{26}$	47.1	41.0	32.6	32.4	26.6	25.9	19.9
$10t_{31}$	46.3	38.0	28.4	29.6	22.0	23.5	16.0
$10t_{41}$	0.99	3.6	5.1	3.5	4.6	2.5	3.4
t_{51}	2123	2078	2279	173	179	2093	1146
t_{52}	640	941	1139	1317	1321	940	569

The experimental results show that with the change of the demagnetizing PMs, the amplitude of each period of induced EMF changes accordingly, but it is difficult to find the characteristic parameters of the corresponding fault types directly. In the time–frequency curve obtained after ST, the amplitude is obviously different, which is convenient for the extraction of characteristic parameters. Table V shows the characteristic parameters corresponding to each fault type extracted from the experimental results. Under the joint action of nine characteristic parameters, the six fault types can be clearly distinguished.

A total of 20 sets of data are collected from each group of faults and are used to verify the accuracy of the classification model, and the results are shown in Fig. 16.

Fig. 16(a) shows the output results of the PSO–LSSVM classification model. Notably, each category is fully distinguished, and the PSO–LSSVM classification model can accurately recognize the PMSLM local demagnetization fault. Fig. 16(b) shows the comparison of the accuracy of the SVM, LSSVM, and PSO–LSSVM classification models. The recognition results of the PSO–LSSVM classification model are nearly consistent with the initial classification results, whereas those of the LSSVM and SVM classification models have evident deviation.

The PSO–LSSVM classification model has the highest accuracy and can better meet the requirements of fault identification compared with the two other models. Therefore, the PMSLM local demagnetization fault classification model established by PSO–LSSVM algorithm effectively ensures the accuracy of fault identification.

The experimental results show that the ST can extract the time–frequency characteristic curves from the original induced EMF signal, which facilitates the extraction of fault characteristic parameters. Comparing the six fault types, the constructed characteristic vector can distinguish each fault type clearly, and

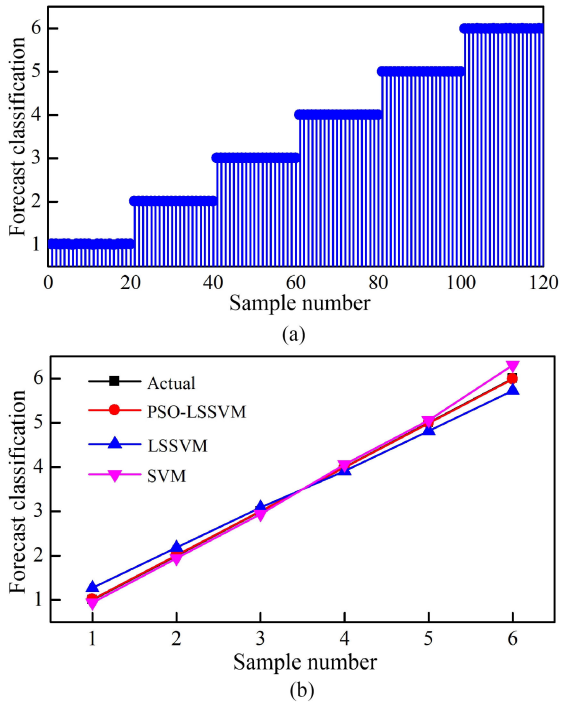

Fig. 16. Classification model accuracy. (a) Output results of the PSO–LSSVM classification model. (b) Comparison of the accuracy of three classification models.

the PSO–LSSVM classification model can recognize each fault type effectively. In summary, the fault diagnosis method based on ST and PSO–LSSVM algorithm can accurately identify the PMSLM local demagnetization faults.

VI. Conclusion

In this article, a method for identifying the PMSLM local demagnetization fault with induced EMF as the fault characteristic signal is studied. The ST is used to decompose the induced EMF in time–frequency domain and extracted the characteristic parameters. Combined with the PSO–LSSVM algorithm, a classification model is established to realize fault identification. For the 14 fault types between 4 pairs of PMs in 2 cycles, the method can accurately identify the position and demagnetization degree of demagnetized PMs. Prototype experiments and simulation experiments are conducted, and the result verified that the proposed method can accurately recognize the PMSLM local demagnetization fault.

References

[1] H. Wang, J. Zhao, J. Zhao, J. Song, Z. Pan, and X. Jiang, "A new rapid-precision position measurement method for linear motor mover based on 1-D EPCA," *IEEE Trans. Ind. Electron.*, vol. 65, no. 9, pp. 7485–7494, Sep. 2018.

[2] M. A. M. Cheema, J. E. Fletcher, D. Xiao, and M. F. Rahman, "A direct thrust control scheme for linear permanent magnet synchronous motor based on on-line duty ratio control," *IEEE Trans. Power Electron.*, vol. 31, no. 6, pp. 4416–4428, Jun. 2016.

[3] Z. He *et al.*, "Thrust ripple reduction in permanent magnet synchronous linear motor based on tuned viscoelastic damper," *IEEE Trans. Ind. Electron.*, vol. 66, no. 2, pp. 977–987, Feb. 2019.

[4] J. Song, F. Dong, J. Zhao, S. Lu, S. Dou, and H. Wang, "Optimal design of permanent magnet linear synchronous motors based on Taguchi method," *IET Elect. Power Appl.*, vol. 11, no. 1, pp. 41–48, 2017.

[5] F. Dong, J. Song, J. Zhao, and J. Song, "Multi-objective design optimization for PMSLM by FITM," *IET Elect. Power Appl.*, vol. 12, no. 2, pp. 188–194, 2018.

[6] Z. Liu, J. Huang, and B. Li, "Diagnosing and distinguishing rotor eccentricity from partial demagnetization of interior PMSM based on fluctuation of high-frequency d-axis inductance and rotor flux," *IET Elect. Power Appl.*, vol. 11, no. 7, pp. 1265–1275, 2017.

[7] D. Joo, J. Cho, K. Woo, B. Kim, and D. Kim, "Electromagnetic field and thermal linked analysis of interior permanent-magnet synchronous motor for agricultural electric vehicle," *IEEE Trans. Magn.*, vol. 47, no. 10, pp. 4242–4245, Oct. 2011.

[8] S. Ruoho, J. Kolehmainen, J. Ikaheimo, and A. Arkkio, "Interdependence of demagnetization, loading, and temperature rise in a permanent-magnet synchronous motor," *IEEE Trans. Magn.*, vol. 46, no. 3, pp. 949–953, Mar. 2010.

[9] C. Zhang *et al.*, "Robust fault-tolerant predictive current control for permanent magnet synchronous motors considering demagnetization fault [J]," *IEEE Trans. Ind. Electron.*, vol. 65, no. 7, pp. 5324–5334, Jul. 2018.

[10] J. C. Urresty, J. R. Riba, and L. Romeral, "A back-emf based method to detect magnet failures in PMSMs," *IEEE Trans. Magn.*, vol. 49, no. 1, pp. 591–598, Jan. 2013.

[11] J. C. Urresty, J. R. Riba, and L. Romeral, "Application of the zero-sequence voltage component to detect stator winding inter-turn faults in PMSMs," *Elect. Power Syst. Res.*, vol. 89, no. 4, pp. 38–44, 2012.

[12] J. Urresty, J. Riba, M. Delgado, and L. Romeral, "Detection of demagnetization faults in surface-mounted permanent magnet synchronous motors by means of the zero-sequence voltage component," *IEEE Trans. Energy Convers.*, vol. 27, no. 1, pp. 42–51, Mar. 2012.

[13] M. Delgado Prieto, A. Garcia Espinosa, J. Riba Ruiz, J. C. Urresty, and J. A. Ortega, "Feature extraction of demagnetization faults in permanent-magnet synchronous motors based on box-counting fractal dimension," *IEEE Trans. Ind. Electron.*, vol. 58, no. 5, pp. 1594–1605, May 2011.

[14] R. Z. Haddad and E. G. Strangas, "On the accuracy of fault detection and separation in permanent magnet synchronous machines using MCSA/MVSA and LDA," *IEEE Trans. Energy Convers.*, vol. 31, no. 3, pp. 924–934, Sep. 2016.

[15] M Ebrahimi B and J Faiz, "Feature extraction for short-circuit fault detection in permanent-magnet synchronous motors using stator-current monitoring," *IEEE Trans. Power Electron.*, vol. 25, no. 10, pp. 2673–2682, Oct. 2010.

[16] J. A. Farooq, A. Djerdir, and A. Miraoui, "Identification of demagnetization faults in a permanent magnet synchronous machine by permeance network," *COMPEL, Int. J. Comput. Math. Elect. Electron. Eng.*, vol. 28, no. 6, pp. 1619–1631, 2009.

[17] Y. S. Lee, K. T. Kim, and H. Jin, "Finite-element analysis of the demagnetization of IPM-type BLDC motor with stator turn fault," *IEEE Trans. Magn.*, vol. 50, no. 2, pp. 889–892, Feb. 2014.

[18] M. H. Holakooie, M. Ojaghi, and A. Taheri, "Full-order Luenberger observer based on fuzzy-logic control for sensorless field-oriented control of a single-sided linear induction motor," *ISA Trans.*, vol. 60, pp. 96–108, 2016.

[19] D. K. Alves, F. B. Costa, R. Lúcio de Araujo Ribeiro, C. Martins de Sousa Neto, and T. de Oliveira Alves Rocha, "Real-time power measurement using the maximal overlap discrete Wavelet-Packet transform," *IEEE Trans. Ind. Electron.*, vol. 64, no. 4, pp. 3177–3187, Apr. 2017.

[20] A. G. Espinosa, J. A. Rosero, J. Cusidó, L. Romeral, and J. A. Ortega, "Fault detection by means of Hilbert–Huang transform of the stator current in a PMSM with demagnetization," *IEEE Trans. Energy Convers.*, vol. 25, no. 2, pp. 312–318, Jun. 2010.

[21] J. Li, Z. Teng, Q. Tang, and J. Song, "Detection and classification of power quality disturbances using double resolution S-transform and DAG-SVMs," *IEEE Trans. Instrum. Meas.*, vol. 65, no. 10, pp. 2302–2312, Oct. 2016.

[22] A. Ahmadimanesh and S. M. Shahrtash, "Transient-based fault-location method for multiterminal lines employing S-transform," *IEEE Trans. Power Del.*, vol. 28, no. 3, pp. 1373–1380, Jul. 2013.

[23] M. Shafiullah and M. A. Abido, "S-transform based FFNN approach for distribution grids fault detection and classification," *IEEE Access*, vol. 6, pp. 8080–8088, 2018.

[24] N. Liu, J. Gao, B. Zhang, F. Li, and Q. Wang, "Time-frequency analysis of seismic data using a three parameters S transform," *IEEE Geosci. Remote Sens. Lett.*, vol. 15, no. 1, pp. 142–146, Jan. 2018.

[25] I. Serrano, O. Deniz, J. L. Espinosa-Aranda, and G. Bueno, "Fight recognition in video using Hough forests and 2D convolutional neural network," *IEEE Trans. Image Process.*, vol. 27, no. 10, pp. 4787–4797, Oct. 2018.
[26] Y. Guo, X. Jia, and D. Paull, "Effective sequential classifier training for SVM-based multitemporal remote sensing image classification," *IEEE Trans. Image Process.*, vol. 27, no. 16, pp. 3036–3048, Jun. 2018.
[27] E. F. D. Oliveira, M. E. D. L. Tostes, and J. C. Leite, "Voltage THD analysis using knowledge discovery in databases with a decision tree classifier," *IEEE Access*, vol. 6, pp. 1177–1188, 2017.
[28] L. Jian, S. Shen, J. Li, X. Liang, and L. Li, "Budget online learning algorithm for least squares SVM," *IEEE Trans. Neural Netw. Learn. Syst.*, vol. 28, no. 9, pp. 2076–2087, Sep. 2017.
[29] Y. Sun, Y. Liu, and H. Liu, "Temperature compensation for a six-axis force/torque sensor based on the particle swarm optimization least square support vector machine for space manipulator," *IEEE Sensors J.*, vol. 16, no. 3, pp. 798–805, Feb. 2016.
[30] N. Huang, X. Liu, D. Xu, and J. Qi, "Power quality disturbances classification based on S-transform and probabilistic neural network," *Neurocomputing*, vol. 98, no. 3, pp. 12–23, 2012.
[31] Q. Wang, J. Gao, N. Liu, and X. Jiang, "High-resolution seismic time-frequency analysis using the synchrosqueezing generalized S-transform," *IEEE Geosci. Remote Sens. Lett.*, vol. 15, no. 3, pp. 374–378, Mar. 2018.
[32] B. Wang and W. Lu, "An efficient amplitude-preserving generalized S transform and its application in seismic data attenuation compensation," *IEEE Trans. Geosci. Remote Sens.*, vol. 56, no. 2, pp. 859–866, Feb. 2018.
[33] S. Bag, A. K. Pradhan, S. Das, S. Dalai, and B. Chatterjee, "S-transform aided random forest based PD location detection employing signature of optical sensor," *IEEE Trans. Power Del.*, vol. 34, no. 4, pp. 1261–1268, Aug. 2019.

Xuewei Song was born in Fuyang, China. She received the M.S. degree in detection technology and automatic equipment from the School of Electrical Engineering, Anhui University, Hefei, China. She is currently working toward the Ph.D. degree in environment oriented information and system engineering with the Graduate School, Mie University, Mie, Japan.

Her current research interests include induction motors and their diagnosis.

Jiwen Zhao was born in Dangshan, China. He received the Ph.D. degree in 2005 from the University of Science and Technology of China, Hefei, China.

Since May, 2019, he has been working with the School of Electrical and Automation Engineering, Hefei University of Technology, Hefei. He is currently a Professor with the School of Electrical and Automation Engineering, Hefei University of Technology. His main research interests include linear motor optimization design and linear motor control.

Juncai Song was born in Huainan, China. He received the B.S. and M.E. degrees in electrical engineering from the Anhui University of Hefei, Hefei, China in 2014 and 2017, respectively. She is currently working toward the Ph.D. degree at the School of Electrical Information Engineering, Anhui University, Hefei, China.

Since 2019, he is a Cooperative, working with the School of Electrical and Automation Engineering, Hefei University of Technology, Hefei, China. His current research interests include design optimization and fault diagnosis in motor.

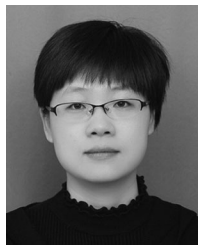

Fei Dong was born in Yuncheng, China. She received the B.S. degree in mechanical engineering from Changan University, Xian, China, in 2006, and the M.S. degree in mechatronic engineering from Changan University, Xian, in 2011.

Since 2011, she has been a Lecturer with the School of Electrical Engineering and Automation, Anhui University, Hefei, China. Her research interests include the design, analysis, and optimization of linear motors.

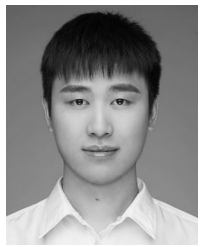

Liang Xu was born in Hefei, China. He received the B.S. degree in mechanical and electrical engineering from Chuzhou University, Chuzhou, China, in 2017. He is currently working toward the M.S. degree in detection technology and automation equipment with the School of Electrical Engineering and Automation, Anhui University, Hefei, China.

His current research interests include fault diagnosis and monitoring of linear motors.

Jing Zhao was born in Huaibei, China. She received the B.S. degree in mechanical engineering from Sichuan University, Chengdu, China, in 2007, and the Ph.D. degree in solid mechanics from the University of Science and Technology of China, Hefei, China, in 2012.

Since 2012, she has been a Lecturer with the School of Electrical Engineering and Automation, Anhui University, Hefei. Her research interests include optical detection, image processing, and high precision motion measurement in linear motor system.